RSC Advances

PAPER

View Article Online
View Journal | View Issue

Check for updates

Cite this: *RSC Adv.*, 2018, **8**, 34536

Stabilization of divalent Eu^{2+} in fluorosilicate glass-ceramics *via* lattice site substitution†

Chenhao Wang,[ab] Xiaotong Chen,[a] Xue Luo,[a] Junjie Zhao,[a] Xvsheng Qiao, *[a] Yong Liu,[a] Xianping Fan, [a] Guodong Qian, [a] Xianghua Zhang[c] and Gaorong Han[a]

Received 15th August 2018
Accepted 17th September 2018

DOI: 10.1039/c8ra06843g

rsc.li/rsc-advances

Fluorosilicate glasses and glass-ceramics with MF_2 (M = Ca, Sr, Ba), ZnF_2 or LaF_3 components were investigated to host divalent Eu^{2+} for photoluminescence (PL) application. X-ray diffraction phase identification and a series of spectroscopic analyses were performed to reveal the relationship between microstructure and the reduction of $Eu^{3+} \rightarrow Eu^{2+}$. The precursor glasses were believed being constituted by silicate-rich phases and fluoride-rich phases, due to the immiscibility of fluoride-and-silicate mixed glass system. After heat treatment, the fluoride-rich glass phases could transform into fluoride crystalline phase in the glass-ceramics. Europium tended to enrich in the fluoride-rich phases in the glasses or in the precipitated fluoride crystalline phases in the glass-ceramics. Small amounts of Eu^{3+} were reduced to Eu^{2+} in the glasses where the electronegativity had a crucial impact. In contrast, large amounts of Eu^{3+} were reduced to Eu^{2+} in the glass-ceramics containing MF_2 nanocrystals, where the reduction was determined by lattice site substitution. Using $ZnAl_2O_4$ containing glass-ceramics as reference, it was evidenced that the similar and a little larger radii between sites and substitution ions are the prerequisite for Eu^{3+}/M^{2+} substitution. And using LaF_3 containing glass-ceramics as reference, it was certified that unbalanced charge at substitution sites induce the $Eu^{3+} \rightarrow Eu^{2+}$ reduction.

Open Access Article. Published on 08 October 2018. Downloaded on 8/27/2025 2:15:17 PM.
This article is licensed under a Creative Commons Attribution-NonCommercial 3.0 Unported Licence.

Introduction

As Eu^{2+} possesses ideal properties for light emission such as large absorption cross section, broad band spectrum, and highly efficient photoluminescence (PL), it has been wildly adopted as active center in phosphor materials.[1,2] Owing to the exposure of 5d-shell of Eu^{2+} to ligands, it is also facile to tune its emission from violet to red by adjusting host lattice.[3] Thus, Eu^{2+}-doped inorganic phosphors have been widely used in commercial lighting and display devices, such as epoxy resin-or-silica mixed phosphor converted light emitting diodes (PC-LED) by mixing with resin or silica as spectrum transfer material.[4] However, such PC-LED structure usually suffers from thermal deterioration because of different thermal expansions and conductivities between phosphors and epoxy resin. In order to solve this problem, researchers recently developed glass-ceramics[5–9] with Eu-doped fluoride crystalline phases. It showed great advantages in thermal resistance, durability, and microstructure manipulation. Eu could enrich in fluoride phase, such as MF_2 (M = Ca, Sr, Ba), of glass-ceramics to adapt itself with well-behaved PL performance.

However, Eu^{2+} and Eu^{3+} always coexist in the host, because Eu cation has variable valences. It thus becomes crucial to keep divalent Eu^{2+} as the majority. Generally, there are several ways to transform Eu^{3+} into Eu^{2+}: (i) adding reducing agents,[10–12] (ii) inputting reducing atmosphere during preparation processes,[13,14] (iii) adjusting optical basicity or electronegativity of host,[15,16] (iv) substituting M^{2+} sites in crystalline lattices.[17,18] As strategies (i) and (ii) accompany drawbacks such as introducing impurities into the system or leading to infeasibility for elaborated optimization of concentration and distribution of Eu^{2+}, strategies (iii) and (iv) are usually considered to be more executable. Using strategy (iv), silicate,[19,20] aluminosilicate,[10,15,21] borophosphate[22,23] and fluoride crystalline phases[24–26] have been reported as good stabilizers for divalent Eu^{2+}. Among them, fluoride crystalline phases show most advantages owing to their ultrasmall sizes down to several nanometers, similar refractive indices with silicate glasses, ideal host to selectively enrich Eu^{2+}. Hence, fluorosilicate glass-ceramics containing Eu^{2+}-enriched fluoride nanocrystals could achieve high transparency, large Eu^{3+}/Eu^{2+} reduction ratio, enhanced PL performance and ideal physico-chemical properties.

Our previous studies[5–7] have evidenced that alkaline earth fluoride (MF_2, where M = Ca; Sr; Ba) nanocrystals could be good hosts to precipitate and enrich Eu^{2+} by Eu^{2+}/M^{2+} lattice substitution. But there is still a lack of systematical dissertation summarizing such lattice substitution strategy for stabilizing

[a]State Key Laboratory of Silicon Materials & School of Materials Science and Engineering, Zhejiang University, Hangzhou 310027, China. E-mail: Qiaoxus@zju.edu.cn

[b]School of Materials Science and Engineering, Tianjin University, Tianjin, 300350, China

[c]Laboratory of Glasses and Ceramics, Institute of Chemical Science UMR CNRS 6226, University of Rennes 1, 35042 Rennes, France

† Electronic supplementary information (ESI) available. See DOI: 10.1039/c8ra06843g

This journal is © The Royal Society of Chemistry 2018

Open Access Article. Published on 08 October 2018. Downloaded on 8/27/2025 2:15:17 PM.
This article is licensed under a Creative Commons Attribution-NonCommercial 3.0 Unported Licence.

Eu^{2+} in the fluorosilicate glass-ceramics. In this study, we prepared glass and glass-ceramic samples with the composition of $50SiO_2$–$20Al_2O_3$–$20MF_2$–$7NaF$–$3EuF_3$ (M = Ca, Sr, Ba, Zn) and $50SiO_2$–$20Al_2O_3$–$20LaF_3$–$7NaF$–$3EuF_3$. By comparative study of the valence state evolution and spectroscopic behaviors of Eu cations, we demonstrate the feasibility of the proposed site substitution strategy to stabilize the divalent Eu^{2+} in the fluorosilicate glass-ceramics containing MF_2 nanocrystals.

Experimental methods

Oxyfluoride glasses (and a glass-ceramic sample) with the compositions of $50SiO_2$–$20Al_2O_3$–$20MF_x$–$7NaF$–$3EuF_3$ in mol%, named as G1–4, GC5 (M = Ca, Sr, Ba, La, or Zn; x is the valence of ion M) was prepared by a melt-quenching method. Total weight of 50 g raw materials was weighed and mixed well in a RETSCH RM 200 mortar grinder. The batches of the raw materials were melted at 1500 °C for 45 min in air. Plain glass was obtained by quenching the melt between two brass plates. The subsequent crystallization temperature of 660 °C was selected between the first crystallization temperature (T_{c1}) and the second crystallization temperature (T_{c2}) for G1–4 (Fig. 1 (a)). The glass-ceramics GC1–4 were obtained by annealing the glasses at the above temperatures for 45 min in air. The compositions and crystallization temperatures of the groups are demonstrated below in Table 1. Note that the ZnF_2-based sample (GC5) loses its transparency due to an uncontrollable crystallization during the melt-quenching process.

Differential thermal analysis (DTA) measurement was carried out on a CDR-1 differential thermal analyzer with fixed specimen weight of 60 mg. XRD analysis was carried out on a PANalytical B.V. Empyrean 200895 X-ray diffractometer with Cu Kα radiation (λ = 1.54 Å), and the scan speed was 2.00 deg min^{-1}. The excitation and emission spectra combining quantum yields were measured by an Edinburgh Instruments fluorospectrometer FLS 920 equipped with a red-sensitive photomultiplier (Hamamatsu R928P) in a Peltier-cooled housing in the single photon counting mode and with the aid of an integration sphere. A 450 W ozone-free xenon lamp was used as the excitation source for steady-state measurements. The calibrations for quantum yields were made by the Edinburgh Instrument and the measurements were repeated three times at room temperature for each excitation scheme and then averaged overall.

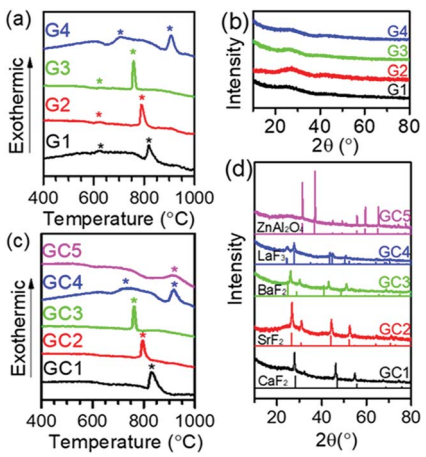

Fig. 1 DTA curves and XRD patterns of the G1–G4 glasses (a and b) and the GC1–GC5 glass-ceramics (c and d) with reference to the standard JCPDS cards.

Table 1 The nominal compositions and the first and second crystallization temperature of glasses

Sample	Composition (mol%)	T_{c1}	T_{c2}
G1	$50SiO_2$–$20Al_2O_3$–$20CaF_2$–$7NaF$–$3EuF_3$	602 °C	800 °C
G2	$50SiO_2$–$20Al_2O_3$–$20SrF_2$–$7NaF$–$3EuF_3$	598 °C	750 °C
G3	$50SiO_2$–$20Al_2O_3$–$20BaF_2$–$7NaF$–$3EuF_3$	597 °C	752 °C
G4	$50SiO_2$–$20Al_2O_3$–$20LaF_3$–$7NaF$–$3EuF_3$	650 °C	882 °C
GC5	$50SiO_2$–$20Al_2O_3$–$20ZnF_2$–$7NaF$–$3EuF_3$	815 °C	

Results and discussion

Transition from glasses to glass-ceramics

Evidenced by differential thermal analysis (DTA, Fig. 1(a and c)) and X-ray diffraction (XRD, Fig. 1(b and d)), sample G1–4 referred to typical inorganic glasses without any crystalline phase, while sample GC5 was glass-ceramic constituted by the precipitated $ZnAl_2O_4$ crystalline phases and residual glass phase. Glass samples G1–G4 have two exothermic DTA peaks, where the first peaks (which appeared at lower temperature) correspond to the precipitation of fluoride nanocrystals (CaF_2, SrF_2, BaF_2, LaF_3). Such kinds of crystalline phases were revealed by XRD patterns (Fig. 1(d)) of the glass-ceramics, GC1–GC4. These samples were obtained by annealing G1–G4 at 660 °C, which were located between two crystallization peaks for 45 minutes. In contrast, the as-melt sample, GC5, was already glass-ceramic with opaque appearance due to the uncontrollable crystallization of $ZnAl_2O_4$ during the quenching process of the melt. According to the Scherrer formula, the crystal sizes could be estimated from peak width of XRD patterns. As a result, the sizes of CaF_2, SrF_2, BaF_2, LaF_3 and $ZnAl_2O_4$ crystals in the glass-ceramics were evaluated as 19.3 ± 0.2 nm, 14.6 ± 0.2 nm, 16.0 ± 0.3 nm, 17.9 ± 2.7 nm and >100 nm, respectively. GC1–4 have high transparency, but GC5 lost its transparency. This is due to much smaller size of precipitated MF_x nanocrystals than the visible-near infrared wavelength, as well as similar refractive indices between MF_x nanocrystals and silicate hosts. So the fluorosilicate glass-ceramics show more optical merits than the reported oxide glass-ceramics.[17–21] The volume fractions of the precipitated nanocrystals (crystallinity) could also be evaluated by the integral intensity ratio of crystalline diffraction to all the diffraction. And the crystallinities were estimated to around 20% for all the glass-ceramic samples. Therefore, the glasses were converted into the glass-ceramics containing CaF_2, SrF_2, BaF_2, LaF_3 nanocrystals except the ZnF_2-based GC5.

Spectroscopic behaviors of Eu^{3+} and Eu^{2+}

The sharp PL peaks in Fig. 2(a and b) were assigned to the 4f–4f transitions of Eu^{3+}, while the broad PL bands in Fig. 2(c) could

Open Access Article. Published on 08 October 2018. Downloaded on 8/27/2025 2:15:17 PM.
This article is licensed under a Creative Commons Attribution-NonCommercial 3.0 Unported Licence.

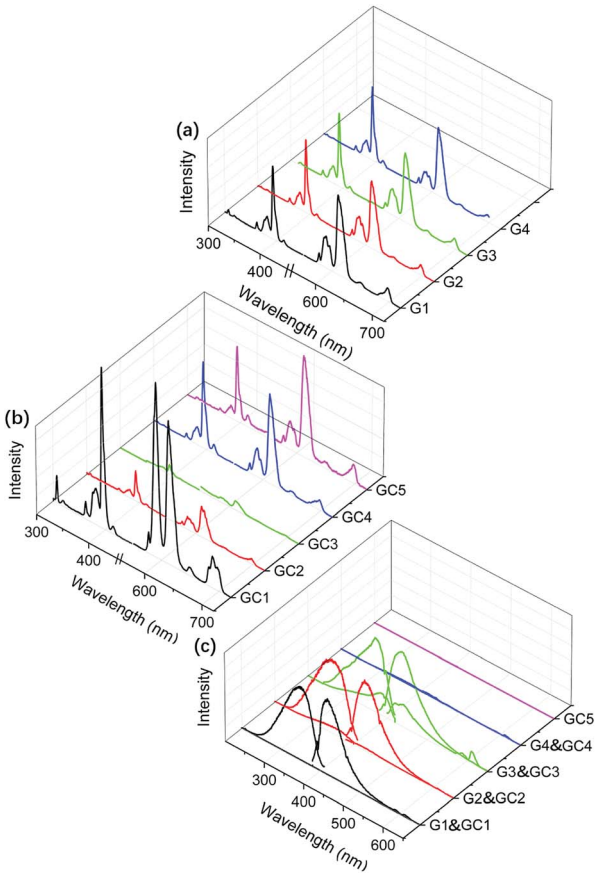

Fig. 2 PL excitation and emission spectra of the glasses (a) and the glass-ceramics (b) by monitoring and exciting with typical 4f–4f transitions of Eu^{3+} ($\lambda_{em} = 612$ nm, $\lambda_{ex} = 393$ nm), where the intensities of the glass in (a) are normalized by the maximum intensities and the intensity of the glass-ceramics in (b) are further normalized by those of the precursor glasses. In contrast, PL spectra (c) of the glasses and glass-ceramics are monitored and excited with typical 4f–5d transitions of Eu^{2+} ($\lambda_{em} = 420$ nm, $\lambda_{ex} = 350$ nm), where all the intensities are normalized by the maximum of the glass-ceramics except that G4, GC4 and GC5 have no intense PL spectra.

be assigned to $4f^7$–$4f^65d^1$ transitions of Eu^{2+}. For Eu^{3+}, the PL excitation peaks of 363, 381, 393 and 414 nm were attributed to the transitions of $^7F_0 \rightarrow {}^5D_4$, $^5G_4$, $^5L_6$, $^5D_3$, respectively. And

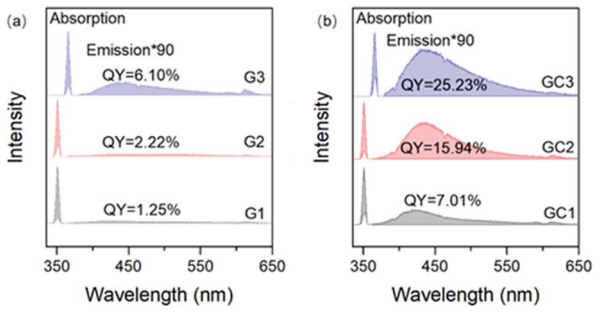

Fig. 3 The integral sphere collected PL spectra of Eu^{2+} in the MF_2-based (a) glasses and (b) glass-ceramics. The excitation spectra were monitored at 350 nm, and the emission spectra were excited at 420 nm.

the PL emission peaks were ascribed to $^5D_0 \rightarrow {}^7F_J$ where $J = 1$, 2, 3 and 4 correspond to 590, 612, 650 and 689 nm, respectively. As the 4f electron shell was shielded by the outer shells (5d and 6s), the 4f–4f transition was less influenced by coordination surroundings, which led the parabolas of $4f^n$ excited states to be located in parallel and directly above the ground state in the configuration coordinate. Therefore, the band widths of Eu^{3+} PL peaks appeared as narrow linear shapes. On the contrary, the PL bands of Eu^{2+} have large band width covering more than 100 nm with the maxima at 350 and 420 nm. As d shell is exposed to ligands, there was offset between the equilibrium position of both the $4f^65d^1$ and $4f^7$ states of Eu^{2+}. Therefore, the f–d transition presented large Stokes shift, and electron–phonon coupling further broadened the PL bands.[27] Such a Stokes shift and spectral broadening are depicted in Fig. S1.† It shows that Eu^{2+} has similar PL bands in the glasses and glass-ceramics. But there are large Stokes shifts on the PL excitation and emission spectra. Between the glass and glass-ceramic samples, more or less Stokes difference exists, where GC3 exhibits the largest Stokes shift (4712 cm^{-1}) among all the samples. These are attributed to the different coordination environments around Eu^{2+} in the glass and glass-ceramics. In the glass samples, Eu^{2+} is mainly surrounded by both O^{2-} and F^-, while Eu^{2+} ions are predominantly enriched in fluoride phase in glass-ceramics. With the enrichment of Eu^{2+} in different nanocrystals, the Stokes shifts of Eu^{2+} also appear to have some differences due to the lattice difference of MF_2 (M = Ca, Sr, Ba) nanocrystals. With configuration coordinates, Fig. S2† illustrates Stokes shift order of Δstokes(G3) < Δstokes(GC3) and Δstokes(G3) < Δstokes(GC1) < Δstokes(GC2).

All the glasses and glass-ceramics showed PL feature of both Eu^{2+} and Eu^{3+}, except that the LaF_3-based samples only exhibited the PL feature of Eu^{3+}. For comparison, the PL intensities of each group were normalized according to glasses for Eu^{3+} and glass-ceramics for Eu^{2+}. Compared to the glasses, most of the glass-ceramics possessed stronger PL for Eu^{2+}, owing to the reduction of Eu^{3+} into Eu^{2+} during the treatment. The Eu^{2+} bands also existed in glass samples and increased by the sequence of G1 to G3 according to Fig. 2(c). The appearance of PL bands implied that reduction of Eu^{3+} started in the glass forming stage. However, the PL of Eu^{3+} displayed intricate changes before and after heat treatment. The Eu^{3+} PL peaks of CaF_2 and LaF_3 based glass-ceramics (GC1 and GC4) strengthened after heat treatment, while the PL peaks of SrF_2 and BaF_2 based glass-ceramics (GC2 and GC3) were weaker than those of the glasses. In addition, sample G4, GC4 and GC5 almost had no intense PL bands of Eu^{2+} according to Fig. 2(c), which indicates the absence of Eu^{2+} in those samples. The evolution of PL intensity could be also evidenced by the integral sphere collected spectra (Fig. 3(a and b)). We believe that the PL behavior of the material was mainly influenced by: (i) the ratio diversification of Eu^{3+}/Eu^{2+} due to the $Eu^{3+} \rightarrow Eu^{2+}$ reduction; (ii) the coordination of Eu^{2+}/Eu^{3+} into the precipitated crystalline phases. These two factors will be discussed in subsequent passages.

This journal is © The Royal Society of Chemistry 2018

Open Access Article. Published on 08 October 2018. Downloaded on 8/27/2025 2:15:17 PM.
This article is licensed under a Creative Commons Attribution-NonCommercial 3.0 Unported Licence.

Electronegativity related reduction of $Eu^{3+} \rightarrow Eu^{2+}$ in the glasses

The reduction of $Eu^{3+} \rightarrow Eu^{2+}$ in glass is usually believed to relate with the optical basicity. This parameter was primarily used to describe the "electron donor ability" of oxygen as well as the concentration of non-bridging oxygen.[28,29] From Fig. 2(c), the PL of Eu^{2+} increased by the consequence of G1 < G2 < G3. However, this trend contradicted the well-developed theory of optical basicity that the lower optical basicity ($\Lambda(Ca^{2+}) < \Lambda(Sr^{2+}) < \Lambda(Ba^{2+})$) determined the higher reduction ratio of Eu^{2+} (G1 > G2 > G3).[15] (Herein, due to relatively small concentration of Eu^{2+}, it could be assumed to still be lower than the PL quenching concentration and thus be correlated with PL intensity.) We believed that the contradiction was primarily because the investigated glasses were fluoride and oxide mixed glass system. Oxide (silicate) glass is covalent bond majored "random tetrahedral network" and linked by sharing corners, while fluoride glass is ionic bond majored "random polyhedral packing" and linked by sharing corners, edges and planes. In the high fluoride content (30 mol%) mixed system, we have revealed that the glass was indeed constructed by separated fluoride-rich glass phases and silicate-rich glass phases.[30] Thus, the $Eu^{3+} \rightarrow Eu^{2+}$ reduction could not be well interpreted by optical basicity, but we tried to relate it with "electronegativity", which was the primary origin of "optical basicity".

Electronegativity, χ, is a chemical property that describes the tendency of an atom or ion to attract electron clouds towards itself.[31] Due to the electronegativity differences between Eu^{3+} and other cations, Eu^{3+} tended to attract more electron density around its neighboring cations with lower electronegativity, and eventually captured an electron from fluorine. Thus, the $Eu^{3+} \rightarrow Eu^{2+}$ reduction was more likely to happen where electronegativity of neighboring cations of Eu^{3+} were lower. In the glass samples, there were indeed two kinds of separated glass phases: fluoride-rich glass phases and silicate-rich glass phases.[30] It has been well evidenced that lanthanides, such as europium, could selectively enrich in fluoride rich phases.[32] According to the "random polyhedral packing" model, $[AlF_6]$ coordination octahedra could form the skeleton of fluoride rich glass phases, and other metal ions such as Ca^{2+}, Sr^{2+}, Ba^{2+} and $Eu^{2+/3+}$ filled the pores of $[AlF_6]$ framework.[33] In G1–G3, the electronegativity decreases as per the sequence $\chi(Ca^{2+}) > \chi(Sr^{2+}) > \chi(Ba^{2+})$, Eu^{2+} ions were more likely to form in the latter groups. In G4, $\chi(Eu^{3+})$ is close to $\chi(La^{3+})$, and in GC5 $\chi(Zn^{2+})$ is much larger than $\chi(Eu^{3+})$, so only slight amounts of Eu^{2+} were found in G4 and no Eu^{2+} was detected in GC5, as shown in Fig. 2(c).

Stabilization of Eu^{2+} in the glass-ceramics *via* lattice site substitution

Lattice site substitution has been considered as a facile Eu^{2+} doping strategy to avoid other impurities, uncontrollable redox reaction and large aggregation. The conversion ratio of reduction through this method was mainly influenced by two crucial factors: the charge and radius of the site. In order to form stable divalent Eu^{2+}, the lattice sites should meet the following criteria: (i) the sites should be originally divalently charged, (ii) the radii of the sites should be close to the radii of Eu^{2+}.[34,35]

The site charge requisition of Eu^{2+} substitution could be examined by comparison between the MF_2 (M = Ca, Sr, Ba)-based (G1, G2, G3) and the LaF_3-based (G4) samples. The crystalline phases of G4 were LaF_3. The trivalent La^{3+} sites rather than divalent ones led to no transition of Eu^{3+} to Eu^{2+} and absence of the Eu^{2+} PL (Fig. 2(c)), although the radii of La^{3+} was close to Eu^{2+} ($R_{La^{3+}}$(1.160 Å) < $R_{Eu^{2+}}$(1.25 Å)). Thus, the divalent sites were required for reduction. As previously reported, the mechanism of the $Eu^{3+} \rightarrow Eu^{2+}$ reduction was expressed by a series of defect equations. When Eu^{3+} enters the lattice containing M^{2+} with similar radii, a cation vacancy with two negative charges is formed

$$3M_M + 2Eu^{3+} \rightarrow 3M^{2+} + 2Eu_M^{\bullet} + V_M'' ; \quad (1)$$

where M_M stands for metal ion which occupied its own lattice, $Eu_M^{\bullet}$ for the doping Eu^{3+} ion which occupied the lattice of metal ion with one extra positive charge, and V_M'' for the vacancy of metal ion with two negative charges.

As the vacancy act as electron donor, Eu^{3+} was reduced to Eu^{2+}.

$$2V_M'' \rightarrow 2V_M^{\times} + 2e' ; \quad (2)$$

$$2e' + 2Eu_M^{\bullet} \rightarrow 2Eu_M^{\times} ; \quad (3)$$

where $V_M^{\times}$ stands for the vacancy of metal ion with no extra charge, $Eu_M^{\times}$ for the doping Eu^{3+} with no extra charge.

These substitution effects were illustrated in Fig. 4. Accordingly, the $Eu^{3+} \rightarrow Eu^{2+}$ reduction took place and alkaline earth cation vacancies formed in GC1–3 (Fig. 4(a–c)), and broad PL bands of Eu^{2+} were found. The lattice constants were calculated by Bragg's Law, as listed in Table 2. The site substitution can be further verified according to lattice constant change. The expansion of CaF_2 lattice in GC1 corresponded with smaller radius of Ca^{2+}(1.12 Å) compared to that of Eu^{2+}(1.25 Å), and the shrinkage of SrF_2/BaF_2 lattice in GC2 and GC3 for larger radii of Sr^{2+}(1.26 Å) and Ba^{2+}(1.42 Å). Also, the Eu^{3+}/La^{3+} substitution took place in LaF_3 lattice of GC4 without the $Eu^{3+} \rightarrow Eu^{2+}$ reduction. The very small deviation from standard lattice constant of LaF_3 in GC4 was due to the very similar radii of La^{3+} (1.160 Å) and Eu^{3+}(1.066 Å).

When the site was divalently charged, the radius difference between substitution cation pairs would play a prime role for the $Eu^{3+} \rightarrow Eu^{2+}$ reduction. By reference to ZnF_2-based sample (GC5), the influence of the radius difference on the lattice site substitution could be clearly observed. The ionic radii[36] with 8 coordination number were demonstrated as below: $R_{Zn^{2+}}$(0.60 Å) < $R_{Eu^{3+}}$(1.066 Å) < $R_{Ca^{2+}}$(1.12 Å) < $R_{Eu^{2+}}$(1.25 Å) < $R_{Sr^{2+}}$(1.26 Å) < $R_{Ba^{2+}}$(1.42 Å). Due to the huge difference between doping cations ($R_{Eu^{3+}}$(1.066); $R_{Eu^{2+}}$(1.25 Å)) and lattice cations ($R_{Zn^{2+}}$(0.60 Å)), a barrier was created in the Eu^{3+}/Zn^{2+} substitution. Moreover, less deviation of $ZnAl_2O_4$ lattice constant in GC5 also confirmed the above theory. Furthermore, the radius differences between Eu^{3+} and M^{2+} sites would determine how much Eu^{3+} would be reduced into Eu^{2+}. The PL intensity of Eu^{2+} increased by the order of GC1 < GC2 < GC3, while that of Eu^{3+}

Open Access Article. Published on 08 October 2018. Downloaded on 8/27/2025 2:15:17 PM.
This article is licensed under a Creative Commons Attribution-NonCommercial 3.0 Unported Licence.

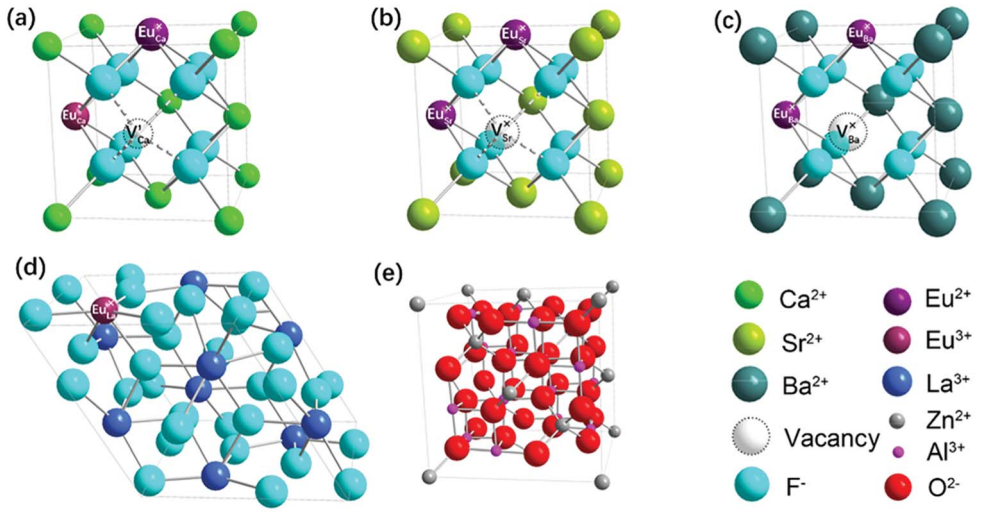

Fig. 4 Schematic model to describe site substitution of Eu^{2+} or Eu^{3+} in different primitive cells. (a–c) Eu^{2+}-doped cubic MF_2 (M = Ca, Sr, Ba) cell, (d) Eu^{3+}-doped hexagonal LaF_3 cell, (e) Eu^{3+}-doped cubic $ZnAl_2O_4$ cell.

decreased by GC1 > GC2 > GC3 (Fig. 2(b)). Thus, the ratio of Eu^{2+}/Eu^{3+} should be GC1 < GC2 < GC3 assuming that the concentrations of Eu^{2+} and Eu^{3+} were lower than the PL quenching concentrations. The $Eu^{3+} \rightarrow Eu^{2+}$ reduction was indeed driven by the radius difference between different Eu^{3+}/M^{2+} pairs. On the one hand, for Eu^{3+}/Ca^{2+} substitution with small radius difference (Ca^{2+}(1.12 Å) *vs.* Eu^{3+}(1.066 Å)) and Ca^{2+} sites with smaller radii than Eu^{2+} (1.25 Å), it only drived Eu^{3+} to be partially reduced to Eu^{2+}, so Eu^{3+}/Eu^{2+} coexisted in GC1. The inversion of PL peak intensities at 590 nm and 612 nm for G1 (Fig. 2(a)) and GC1 (Fig. 2(b)) well verified the CaF_2 crystalline coordination environment of Eu^{3+} in GC1. The PL enhancement of Eu^{3+} (Fig. 2(b)) was due to lower phonon energy and lower multi-phonon transition ratio of Eu^{3+} in CaF_2 lattice of GC1. As both the Eu^{3+} and Eu^{2+} were enriched in the CaF_2 nano-crystals, the strengthened cross relaxation transition between Eu^{2+}/Eu^{3+} coincidentally eliminated the weakening of multi-phonon transition, so the PL lifetime of GC1 had no significant change compared to G1 (Fig. 5 and Table 3). On the other hand, Eu^{3+}/Ba^{2+} or Eu^{3+}/Sr^{2+} substitution with large radius difference (Sr^{2+}(1.26 Å)/Ba^{2+}(1.42 Å) *vs.* Eu^{3+}(1.066 Å)) and Sr^2/Ba^{2+} sites with larger radii than Eu^{2+}(1.25 Å) drived more Eu^{3+} to be reduced to Eu^{2+}. Accordingly, large amounts of Eu^{3+} remained trivalent in GC1, while small amounts remained in GC2 and GC3. No inversion of PL peak intensities at 590 nm and 612 nm for G2 and G3 (Fig. 2(a)) and GC2 and GC3 (Fig. 2(b)) implied that all Eu^{3+} in GC2 and GC3 corresponded to those remaining in the glassy phase, which exhibited much shorter PL lifetimes (Fig. 5; Table 3).

Quantum yield (QY) improvement and PL enhancement of Eu^{2+}

After heat treatment, large quantities of Eu^{2+} formed by Eu^{3+}/M^{2+} substitution in GC1–GC3, QY of the Eu^{2+} PL (Fig. 3) was improved to about 4–7 times of QY of precursor glasses. QY is dominated by two competitive processes: radiative transition (RT) and non-radiative transition (NRT). Theoretically, the probability of RT and NRT, W_{RT} and W_{NRT} have the following relationships:

$$\tau = \frac{1}{W_{RT} + W_{NRT}}; \quad (4)$$

$$\eta = \frac{W_{RT}}{W_{RT} + W_{NRT}} = \tau W_{RT}; \quad (5)$$

where η and τ represent QY and lifetime of PL, respectively. Accordingly, the QY improvement depended on lower NRT or longer PL life time. Eu^{2+} ions were mainly enriched in the separated fluoride glass phases filled with large content of quenching defects, unsaturated bonds and interfaces. Thus,

Table 2 The calculated lattice constants and standard values of precipitated nanocrystals in glass-ceramics

Crystalline phase	Lattice constant (Å)	Standard value (Å)
CaF_2 in GC1	5.545	5.463 (PDF#35-0816)
SrF_2 in GC2	5.760	5.800 (PDF#06-0262)
BaF_2 in GC3	5.929	6.200 (PDF#04-0452)
LaF_3 in GC4	7.184 × 7.184 × 7.351	7.187 × 7.187 × 7.35 (PDF#32-0483)
$ZnAl_2O_4$ in GC5	8.072	8.089 (PDF#05-0669)

This journal is © The Royal Society of Chemistry 2018

Open Access Article. Published on 08 October 2018. Downloaded on 8/27/2025 2:15:17 PM.
This article is licensed under a Creative Commons Attribution-NonCommercial 3.0 Unported Licence.

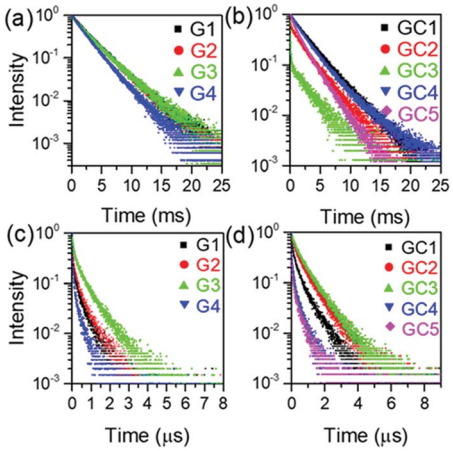

Fig. 5 PL Decay curves of samples. (a and b) the glass and glass-ceramics samples excited at 393 nm and monitored at 612 nm for Eu^{3+} (c and d) Excited at 350 nm and monitored at 420 nm for Eu^{2+}.

Table 3 The lifetime of luminescence emitted by Eu^{2+} and Eu^{3+}

Sample	Eu^{3+} (μs)	Eu^{2+} (ns)	Sample	Eu^{3+} (μs)	Eu^{2+} (ns)
G1	3.06	174	GC1	3.03	321
G2	3.29	206	GC2	2.32	476
G3	3.08	342	GC3	1.77	612
G4	2.48	112	GC4	2.58	168
			GC5	1.96	85

Eu^{2+} in the glasses had high W_{RT} and low QY (<10%), which was also evidenced by the shorter lifetimes of Eu^{2+} (Fig. 5(c)). On the contrary, Eu^{2+} in the glass-ceramics were incorporated in MF_2 crystalline phases, where the concentration of PL quenching centers were much lower than those in glass phases. Therefore, PL lifetimes of Eu^{2+} in the glass-ceramics (Fig. 5(d)) appeared much longer than those of the precursor glasses. It supports the glass-ceramics, GC1–GC3, achieved much higher QY of the Eu^{2+} PL.

Besides a high QY value, strong PL still requires high concentration of the active center (Eu^{2+}) without serious concentration quenching. The BaF_2-based glass-ceramics possessed high solubility of Eu^{2+} rather than SrF_2 or CaF_2-based glass-ceramics. Larger radii as well as large radius difference were found to play almost equal roles when reducing Eu^{3+} into Eu^{2+}. Therefore, the BaF_2-based rather than the SrF_2-based glass-ceramics got the highest QY and the strongest PL, simultaneously. It also demonstrates that the proposed MF_2 lattice site substitution strategy is very suitable for alkaline earth fluorosilicate glass-ceramics showing great advantages in large amount (3–5 mol%) of Eu introduction, high reduction ratio of Eu^{3+}/Eu^{2+} than in other hosts and efficiently enhanced PL of Eu^{2+} compared to that of oxide glass-ceramics.[19–23]

We also evaluate the reproducibility and applicability of the present lattice substitution method for fabrication of Eu^{2+}-doped fluorosilicate glass-ceramics. From Fig. S3,† it is evidenced that the glass-ceramics could be well reproduced with a highly similar PL bands and the PL performance could also be well maintained even after 3 years. Moreover, the lattice substitution strategy primarily relies on the annealing processes, which has been widely applied in the glass and ceramic industry. Therefore, the proposed preparation method has good applicability in large scale applications.

Conclusions

The separated fluoride glass phases formed in the precursor fluorosilicate glasses transformed into fluoride nanocrystals in the glass-ceramics after heat treatment. The inclined precipitation of alkaline earth fluoride nanocrystals and the Eu^{3+}/M^{2+} lattice site substitution enabled the facile $Eu^{3+} \rightarrow Eu^{2+}$ reduction and stabilization of Eu^{2+} in the fluorosilicate glass-ceramics. The Eu tended to enrich in fluoride-rich phases of the glasses and in the fluoride nanocrystalline phases of the glass-ceramics. In glasses, the $Eu^{3+} \rightarrow Eu^{2+}$ reduction depended on the electronegativity of fluoride glass phases, while in glass-ceramics, the $Eu^{3+} \rightarrow Eu^{2+}$ reduction depended on the lattice site substitution in fluoride crystalline phases. The lattice site substitution depended on two key factors: the radii and the valency difference between sites and substitution ions. The similar radii between sites and ions were the prerequisites of the doping. Too small radii of doping ions (like Zn^{2+}) were not preferred for Eu^{3+}/M^{2+} substitution, while comparably larger radii (like Ba^{2+}) were more facile for both Eu^{3+}/M^{2+} substitution and $Eu^{3+} \rightarrow Eu^{2+}$reduction. And to some extent, larger the radii, easier it was for the Eu^{3+}/M^{2+} substitution to take place. The unbalanced charge at the substitution sites drived the reduction of $Eu^{3+} \rightarrow Eu^{2+}$. The Eu^{3+}/M^{2+} substitution was attributed to the $Eu^{3+} \rightarrow Eu^{2+}$ reduction, while Eu^{3+}/La^{3+} substitution led to almost no reduction of Eu^{3+}. High Eu^{2+} doping concentration and enhanced luminescent QY of Eu^{2+} were simultaneously achieved in BaF_2-based glass-ceramic.

Conflicts of interest

There are no conflicts to declare.

Acknowledgements

The authors gratefully acknowledge the financial support from the National Key Research and Development Program of China (No. 2016YFB0303700), the National Nature Science Foundation of China (No. 51672243), Zhejiang Provincial Natural Science Foundation of China (No. LY16E020003), the Fundamental Research Funds for the Central Universities (No. 2016QNA4005; No. 2016FZA4007).

Notes and references

1 P.-P. Dai, C. Li, X.-T. Zhang, J. Xu, X. Chen, X.-L. Wang, Y. Jia, X. Wang and Y.-C. Liu, *Light: Sci. Appl.*, 2016, **5**, E16024.
2 Y. H. Kim, P. Arunkumar, B. Y. Kim, S. Unithrattil, E. Kim, S.-H. Moon, J. Y. Hyun, K. H. Kim, D. Lee, J.-S. Lee and W. B. Im, *Nat. Mater.*, 2017, **16**, 543–550.

Open Access Article. Published on 08 October 2018. Downloaded on 8/27/2025 2:15:17 PM.
This article is licensed under a Creative Commons Attribution-NonCommercial 3.0 Unported Licence.

3 X. Zhang, J. Wang, L. Huang, F. Pan, Y. Chen, B. Lei, M. Peng and M. Wu, *ACS Appl. Mater. Interfaces*, 2015, **7**, 10044–10054.
4 S. Ye, F. Xiao, Y. X. Pan, Y. Y. Ma and Q. Y. Zhang, *Mater. Sci. Eng., R*, 2010, **71**, 1–34.
5 Q. Luo, X. Qiao, X. Fan, S. Liu, H. Yang and X. Zhang, *J. Non-Cryst. Solids*, 2008, **354**, 4691–4694.
6 Q. Luo, X. Qiao, X. Fan and X. Zhang, *J. Am. Ceram. Soc.*, 2010, **93**, 2684–2688.
7 Q. Luo, X. Fan, X. Qiao, H. Yang, M. Wang and X. Zhang, *J. Am. Ceram. Soc.*, 2009, **92**, 942–944.
8 J. Fu, J. M. Parker, P. S. Flower and R. M. Brown, *Mater. Res. Bull.*, 2002, **37**, 1843–1849.
9 L. Zur, J. Janek, M. Soltys, T. Goryczka, J. Pisarska and W. A. Pisarski, *J. Non-Cryst. Solids*, 2016, **431**, 145–149.
10 Y. Gao, J. Qiu and D. Zhou, *J. Am. Ceram. Soc.*, 2017, **100**, 2901–2913.
11 T. Grzyb, A. Szczeszak, Z. Sniadecki, B. Idzikowski and S. Lis, *J. Alloys Compd.*, 2016, **686**, 489–495.
12 G. Chen, L.-J. Yin, J.-T. Dong, Y.-Y. Feng, Y. Gao, W. He, Y. Jia, X. Xu and H. T. Hintzen, *J. Am. Ceram. Soc.*, 2016, **99**, 183–190.
13 H. Bian, Y. Liu, D. Yan, H. Zhu, C. Liu, C. Xu, X. Wang and H. Zhang, *J. Am. Ceram. Soc.*, 2017, **100**, 3467–3477.
14 M. Nogami, A. Koiwai and T. Nonaka, *J. Am. Ceram. Soc.*, 2016, **99**, 1248–1254.
15 S. Liu, G. Zhao, W. Ruan, Z. Yao, T. Xie, J. Jin, H. Ying, J. Wang and G. Han, *J. Am. Ceram. Soc.*, 2008, **91**, 2740–2742.
16 H. Wang, S. Ye, S. Li, T. Liu, J. Lin and D. Wang, *J. Alloys Compd.*, 2015, **648**, 13–17.
17 W. Chen, X. Chen, F. Sun and X. Wang, *J. Alloys Compd.*, 2017, **698**, 565–570.
18 C. Zhu, D. Wu, Y. Zhang, M. Zhang and Y. Yue, *J. Alloys Compd.*, 2015, **632**, 291–295.
19 G. Gao, N. Da, S. Reibstein and L. Wondraczek, *Opt. Express*, 2010, **18**(suppl. 4), A575–A583.
20 G. Gao, S. Reibstein, M. Peng and L. Wondraczek, *J. Mater. Chem.*, 2011, **21**, 3156.
21 H. Bouchouicha, G. Panczer, D. de Ligny, Y. Guyot, M. L. Baesso, L. H. C. Andrade, S. M. Lima and R. Ternane, *J. Lumin.*, 2016, **169**, 528–533.
22 K. Qiu, S.-c. Xu, H. Tian, X. Zheng, T.-s. Lv, Q.-f. Lu and D.-j. Wang, *Optoelectronics Letters*, 2011, **7**, 350–353.
23 C. Zhu, Y. Yang, X. Liang, S. Yuan and G. Chen, *J. Am. Ceram. Soc.*, 2007, **90**, 2984–2986.
24 Y. Jiang, P. Zhang, T. Wei, J. Fan, B. Jiang, X. Mao and L. Zhang, *RSC Adv.*, 2016, **6**, 55366–55373.
25 K. Biswas, A. D. Sontakke and K. Annapurna, *Int. J. Appl. Glass Sci.*, 2012, **3**, 154–162.
26 B. Henke, C. Passlick, P. Keil, J. A. Johnson and S. Schweizer, *J. Appl. Phys.*, 2009, **106**, 113501.
27 G. Blasse and B. C. Grabmaier, *Luminescent Materials*, Springer-Verlag, Berlin Heidelberg, 1997.
28 J. A. Duffy and M. D. Ingram, *J. Inorg. Nucl. Chem.*, 1976, **38**, 1831–1833.
29 J. A. Duffy, *J. Non-Cryst. Solids*, 1989, **109**, 35–39.
30 J. Zhao, R. Ma, X. Chen, B. Kang, X. Qiao, J. Du, X. Fan, U. Ross, C. Roiland, A. Lotnyk, L. Kienle and X. Zhang, *J. Phys. Chem. C*, 2016, **120**, 17726–17732.
31 W. L. Jolly, in *Modern Inorganic Chemistry*, McGraw-Hill, New York, 2nd edn, 1991, pp. 71–76.
32 D. Chen, Z. Wan, Y. Zhou, P. Huang, X. Zhou, Y. Yu, J. Zhong, M. Ding and Z. Ji, *J. Eur. Ceram. Soc.*, 2016, **36**, 679–688.
33 M. E. Lines, *Phys. Rev. B: Condens. Matter Mater. Phys.*, 1980, **21**, 5793–5801.
34 C. Zhu, Y. Yang, X. Liang, S. Yuan and G. Chen, *J. Am. Ceram. Soc.*, 2007, **90**, 2984–2986.
35 Z. Lian, J. Wang, Y. Lv, S. Wang and Q. Su, *J. Alloys Compd.*, 2007, **430**, 257–261.
36 R. D. Shannon, *Acta Crystallogr., Sect. A: Cryst. Phys., Diffr., Theor. Gen. Crystallogr.*, 1976, **32**, 751–767.

This journal is © The Royal Society of Chemistry 2018